AGU PUBLICATIONS

JGR

Journal of Geophysical Research: Space Physics

RESEARCH ARTICLE
10.1002/2013JA019255

Key Points:
- An ionospheric flow shear is associated with the preexisting auroral arc
- The FAC of the PAA is primarily closed by N-S Pedersen current in the ionosphere
- The PAA is located very close to the R1/R2 boundary

Supporting Information:
- Readme
- Appendix S1

Correspondence to:
F. Jiang,
fjiang@igpp.ucla.edu

Citation:
Jiang, F., M. G. Kivelson, R. J. Strangeway, K. K. Khurana, and R. Walker (2015), Ionospheric flow shear associated with the preexisting auroral arc: A statistical study from the FAST spacecraft data, *J. Geophys. Res. Space Physics*, *120*, 5194–5213, doi:10.1002/2013JA019255.

Received 26 JUL 2013
Accepted 6 APR 2015
Accepted article online 8 APR 2015
Published online 24 JUN 2015

©2015. American Geophysical Union. All Rights Reserved.

Ionospheric flow shear associated with the preexisting auroral arc: A statistical study from the FAST spacecraft data

Feifei Jiang[1], Margaret G. Kivelson[1,2], Robert J. Strangeway[1], Krishan K. Khurana[1], and Raymond Walker[1,3]

[1]Department of Earth, Planetary and Space Sciences, University of California, Los Angeles, California, USA, [2]Department of Atmospheric, Oceanic and Space Sciences, University of Michigan, Ann Arbor, Michigan, USA, [3]National Science Foundation, Arlington, Virginia, USA

Abstract An auroral substorm is a disturbance in the magnetosphere that releases energy stored in the magnetotail into the high-latitude ionosphere. By definition, an auroral substorm commences when a discrete auroral arc brightens and subsequently expands poleward and azimuthally. The arc that brightens is usually the most equatorward of several auroral arcs that remain quiescent for ~5 to ~60 min before the breakup commences. This arc is often referred to as the "preexisting auroral arc (PAA)" or the "growth-phase arc." In this study, we use FAST measurements to establish the statistics of flow patterns near PAAs in the ionosphere. We find that flow shear is present in the vicinity of a preexisting arc. When a PAA appears in the evening sector, enhanced westward flow develops equatorward of the arc, whereas when a PAA appears in the morning sector, enhanced eastward flow develops poleward of the arc. We benchmark locations of the PAAs relative to large-scale field-aligned currents (FACs) and convective flows in the ionosphere, finding that the arc forms in the upward current region within ~1° of the Region 1/Region 2 boundary in all local time sectors from 20 MLT to 03 MLT. We also find that near midnight in the Harang region, most of the PAAs lie within 0.5° poleward of the low-latitude Region 1/Region 2 currents boundary and sit between the westward and eastward flow peak but equatorward of the flow reversal point. Finally, we examine arc-associated electrodynamics and find that the FAC of the PAA is mainly closed by the north-south Pedersen current in the ionosphere.

1. Introduction

Auroral substorms were first described more than 40 years ago, and their ionospheric and magnetospheric signatures have been investigated extensively. In optical images, auroral substorms involve brightening of a discrete arc followed by poleward and azimuthal expansion. The arc that brightens is usually the most equatorward of several auroral arcs that remain quiescent for ~5 to ~60 min before the breakup commences [e.g., *Akasofu*, 1964].

Although brightening and subsequent poleward expansion of a quiet preexisting arc is an indisputable signature of an auroral substorm, the magnetospheric generator that drives the current system of such an arc remains unclear. The MHD momentum equation, $\rho \frac{d\mathbf{U}}{dt} = \mathbf{J} \times \mathbf{B} - \nabla P$ (ρ is density, **U** is the averaged flow velocity, **J** is current density, **B** is magnetic field, and P is plasma pressure), requires that the $\mathbf{J} \times \mathbf{B}$ force be balanced by the forces arising from pressure gradients and variation of momentum. Further analysis indicates that field-aligned current (FAC) flows out of the magnetosphere if surfaces of constant pressure are not aligned with magnetic shells or if flow shear exists [*Vasyliunas* 1970]. While the connection between the preexisting auroral arc (PAA) and magnetospheric pressure gradients has been discussed [e.g., *Mende et al.*, 2012], no studies have looked at the relationship between flow shear and the source of the PAA before substorm onset. Therefore, it is the objective of this study to investigate whether a flow shear is related to the PAA.

Searching directly for a flow shear in the source region of the PAA is challenging for two reasons. First, the magnetospheric source of the PAA is a localized region within the vast expanse of the magnetotail. Even a few satellites provide relatively sparse sampling of the region to which the auroral zone maps. Second, empirical magnetic field models that link magnetospheric signatures to their ionospheric footprints

become inaccurate tailward of the regions in which the Earth's dipolar magnetic field is dominant (beyond ~8 R_E), in the region to which the PAA is estimated to be magnetically conjugate. Consequently, in this work, we investigate the relationship between flow shear and the PAA by establishing the flow patterns near a preexisting arc in the ionosphere. The properties of ionospheric flows are relevant to the magnetospheric source, because any magnetospheric flow would produce an ionospheric counterpart that can be easily measured from radar, rockets, or low-altitude spacecraft, outside of the region of field-aligned potential drop and within the PAA. The ionospheric signatures in turn provide clues to the arc's source in the tail.

The electrodynamic pattern associated with discrete arcs independent of substorm phases has been examined extensively by rockets [*Marklund* 1984; *Brüning et al.,* 1985], by satellites [*Heelis et al*., 1981], and by radars [*de la Beaujardière et al.,* 1977, 1981; *Stiles et al*., 1980; *Vondark* 1981]. *Marklund* [1984] used these experimental results, in addition to rocket observations, to organize auroral arc types based on the arc-associated electric field patterns. Later, *Timofeev and Galperin* [1991] selected published observations of longitudinally extended auroral arcs with life time more than 1000 s, measured in the equatorward and central part of the auroral oval under steady conditions, to investigate arc-associated electrodynamics. They found that the electric field pattern associated with these quasi-steady arcs is consistent with that of an "evening arc" in *Marklund* [1984], in which the strength of the north-south (N-S) electric field in the downward FAC region adjacent to an arc increases. They found that the increase is seen equatorward of the arc in the evening region and poleward of the arc in the morning region. These results imply increased westward flow equatorward of an auroral arc in the evening sector and increased eastward flow poleward of an auroral arc in the morning sector.

It is now understood that increased electric field (azimuthal flow) is expected to be seen adjacent to an auroral arc in the ionosphere as a result of current continuity (we will address this in detail in section 5). Previous studies on auroral arc electrodynamics such as those listed above were conducted on case-by-case basis, and there has yet to be a statistical study that characterizes the electric field/flow pattern around the PAA prior to a substorm. A key remaining question is as follows: Is the flow pattern in the vicinity of the PAA similar to that reported in earlier studies [e.g., *Timofeev and Galperin*, 1991]? What is the magnitude and spatial scale of the flow shear associated with the PAA?

In order to understand the ionospheric flow associated with an auroral arc, we require simultaneous measurements of the location of the PAA and of the flow or the electric field in its vicinity. We are able to identify these critical features in data from a low-altitude spacecraft. In this study, FAST data [*Harvey et al*., 2001; Paschmann et al., 2003, and references therein] are used to investigate the electric field/flow pattern around PAAs in the ionosphere. In the next section, the FAST data and the criteria used to identify PAAs in the ionosphere are introduced. Our statistical results are based on properties of all the events identified by this analysis. In section 3, we describe in detail two events in which FAST crossed a PAA during a substorm growth phase, with one case in the premidnight sector and the other in the postmidnight sector. Section 4 presents a statistical analysis of FAST data to characterize typical location of PAAs relative to large-scale FACs and convective flows and also to establish the electrodynamics pattern associated with PAAs. Our work is summarized in section 5.

2. FAST Data and Event Selection

In order to investigate the flow pattern around a PAA, it would be desirable to use optical images to identify a preexisting arc during an interval when a low-altitude spacecraft is passing over it and measuring the plasma flow or, equivalently, the electric field. The low-altitude FAST satellite provides data with sufficiently high spatial/temporal resolution to resolve the fine structure of the electric field associated with a thin PAA (~10 km). Since 2006, the THEMIS all-sky imager array has been providing systematic imaging of auroral activity. Unfortunately, the electric field measurements on FAST were reliable only before 2001. Consequently, one cannot carry out the analysis using conjugate observations from these two datasets. Nevertheless, we have learned many features of the PAA from previous studies that used low-altitude spacecraft particle and magnetometer data at times when optical images were available. These features enable us to identify the location of a PAA from spacecraft particle measurements without auroral images. It is known that the PAA is typically the most equatorward discrete arc present during the growth phase or a quiescent time prior to substorm onset [e. g., *Akasofu* 1964]. The PAA is usually embedded within a

region of increased ion precipitation with an energy range between ~1 keV and ~20 keV in the premidnight sector [e.g., *Samson et al.*, 1992] and somewhat poleward of the inner edge of the electron plasma sheet. In addition, observations show that the precipitating electrons associated with the preexisting arc are accelerated by field-aligned potential drops [e.g., *Lessard et al.*, 2007; *Jiang et al.*, 2012]. These characteristics support the use of the following criteria to identify the presence of a PAA from spacecraft data alone:

1. In the electron energy spectra, FAST should record increased electron precipitation consistent with field-aligned acceleration, i.e., more intense electron fluxes in the downward direction than in the upward direction.
2. The enhanced electron precipitation associated with the PAA structure should be monoenergetic, as contrast to diffuse or broadband precipitation. To quantify monoenergetic precipitation, we adopt the criteria established from 10 years of DMSP data in *Newell et al.* [2009], in which three standards are used to characterize monoenergetic precipitation:

a The differential energy flux of the monoenergetic precipitation must exceed 10^8 eV/(s-str-eV-cm^2) at the peak energy channel. This value corresponds to flux at DMSP altitude, and in this work we retain it as a threshold for flux at FAST altitude.

b The energy at which the differential energy flux peaks should be above 100 eV, and the average energy of the enhanced electron precipitation should be above 80 eV.

c If the differential energy flux peaks at energy W_0, we require the differential energy flux to drop to 30% or less of the peak energy flux in the energy range between 0.5 W_0 and 2 W_0. For the FAST ESA instrument, consecutive energy bins are separated by a factor of ~1.2. Therefore, we require that the differential energy flux needs to drop to 30% or less of the peak energy flux within four channels below and above the peak energy channel.

3. The peak precipitating electron energy flux of the PAA structure should exceed 0.2 erg/cm^2/s at auroral altitude (110 km above the earth). For the green line emission, 0.2 erg/cm^2/s roughly corresponds to 200 Rayleigh, which is close to the luminosity of airglow. This ensures that the luminosity of the arc-associated electron precipitation exceeds the background brightness as well as the sensitivity of the THEMIS white light camera (~100 Rayleigh).
4. The PAA is the most equatorward monoenergetic electron precipitation structure that is embedded within the electron plasma sheet but poleward of its inner edge.
5. The PAA is encountered during a quiescent time or growth phase within 1 h prior to a substorm as inferred from the *AL* index. We select the 1 h time window to improve statistics after testing that arc properties do not seem to change if we extend the time window from 30 min to 1 h.
6. The PAA is encountered by FAST in the MLT range between 20 and 03. *Wang et al.* [2007] examined the substorm onset locations from the FUV imagers on the IMAGE spacecraft and found that for southward IMF intervals, the MLT distribution of onset location peaks at 23 with a standard deviation of 2.6. Thus, the most likely substorm onset MLT lies between 20.4 and 1.6. In optical images, the preexisting arc recorded by the THEMIS all-sky imagers typically has an azimuthal extent of 2–3 MLT h [e.g., *Nishimura et al.*, 2011; *Jiang et al.*, 2012]. Therefore, 20 MLT and 3 MLT are selected as the westward and eastward endpoints of the PAA.

Criteria 1–3 ensure that the PAA structure identified from the FAST particle data has the properties of an auroral arc that is bright enough to be imaged by a camera. One should bear in mind that criterion 2(c) requires significant enhancement of energy flux in a narrow energy band, and sometimes it can be too strict to include electron precipitation that is actually an arc. Criteria 4–6 ensure that the PAA structure has the specific properties of a growth-phase arc leading to auroral breakup. Because the indirect evidence used to infer the presence of the PAA could misidentify some events, a large database of FAST measurements is required for meaningful statistics. Fortunately, our manual survey of FAST data from January 1998 to June 1999 yielded ~180 events that meet the selection criteria (listed in the supporting information Appendix S1). We describe two examples next and then discuss the statistics of the complete set of events.

3. Two Case Studies of "PAAs" Observed by FAST

3.1. A Postmidnight Event

Figure 1a displays FAST data from a pass across the nightside auroral oval near 1.2 MLT in the northern hemisphere on 20 May 1999. Panels from top to bottom are electron energy flux spectra over an energy range from 5 eV to 28 keV with a pitch angle range from (a) 0° to 30°, (b) 60° to 120°, and (c) 150° to 180°;

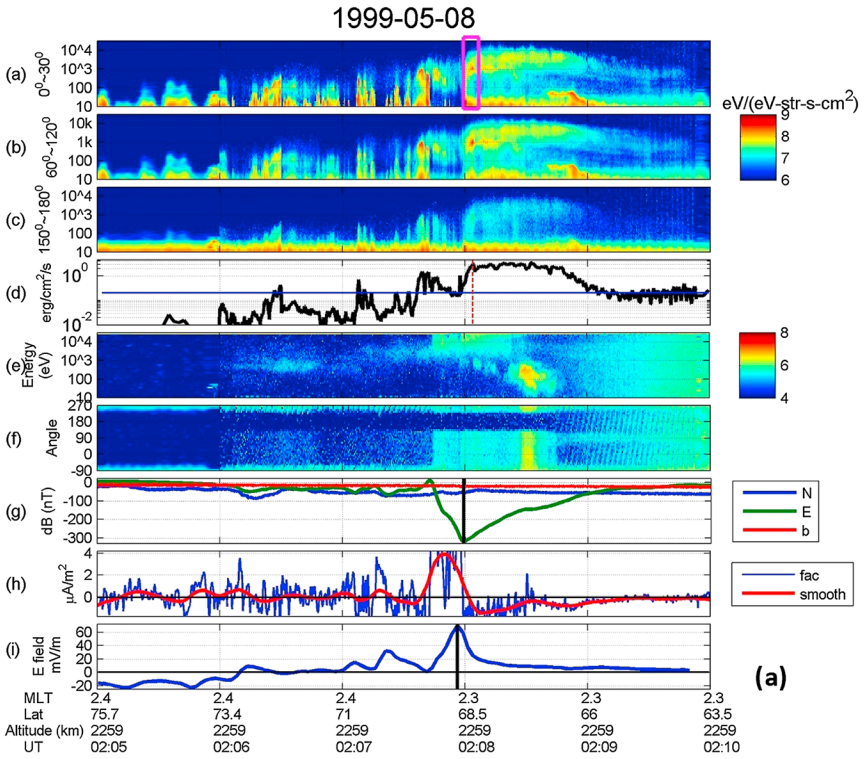
1999-05-08
(a)
(b)
(c)
(d)
(e)
(f)
(g)
(h)
(i)
eV/(eV-str-s-cm2)
N
E
b
fac
smooth
MLT
Lat
Altitude (km)
UT
(a)

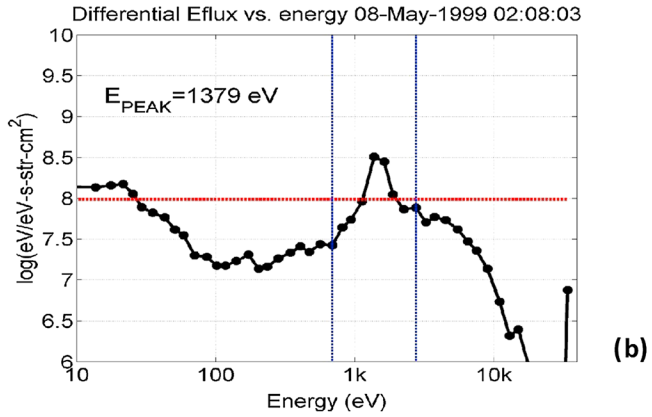
Differential Eflux vs. energy 08-May-1999 02:08:03
EPEAK=1379 eV
log(eV/eV-s-str-cm2)
Energy (eV)
(b)

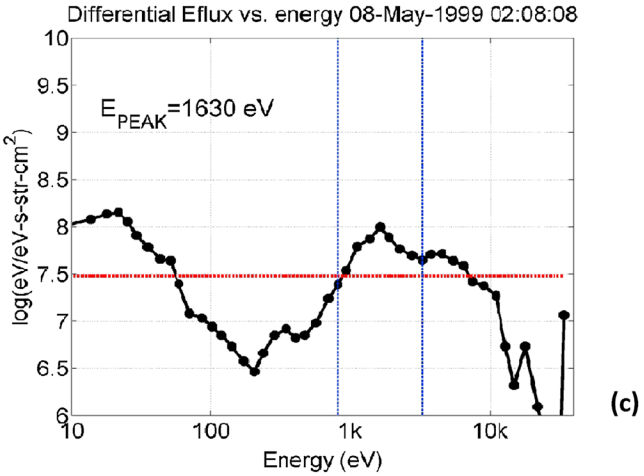
Differential Eflux vs. energy 08-May-1999 02:08:08
EPEAK=1630 eV
log(eV/eV-s-str-cm2)
Energy (eV)
(c)

Figure 1

(d) electron precipitating energy flux mapped to 110 km above the earth; (e) ion omnidirectional energy flux over an energy range from 10 eV to 27 keV; (f) ion energy flux versus pitch angle for all energies; (g) three components of the perturbation magnetic field in the background field-aligned coordinate system; (h) amplitude of the FAC density derived from magnetic field perturbations using Ampere's law; and (i) electric field in the plasma corotation frame and along the direction (north-south) of spacecraft motion. The MLT, invariant latitude, altitude, and UT are indicated below the panels. In Figure 1d the precipitating electron energy flux at FAST altitude is calculated by integrating the differential energy flux over 100 eV to 34000 eV (upper bound of the ESA instrument energies) and over the local loss cone angle:

$$E_{\text{flux}}^{\text{FAST}} = \int E_{\text{flux}} \cos\theta \mathrm{d}E\mathrm{d}\Omega = 2\pi \int_{0}^{\alpha_{\text{loss}}} \int_{100\text{ eV}}^{34{,}000\text{ eV}} E_{\text{flux}} \cos\theta \sin\theta \mathrm{d}\theta \mathrm{d}E \tag{1}$$

Here 100 eV is adopted as the lower bound in the integral to exclude flux associated with secondary electrons. The local loss cone angle α_{loss} is calculated as $\alpha_{\text{loss}} = \arcsin\frac{B^{\text{FAST}}}{B^{\text{aurora}}}$, where B^{FAST} is the magnetic field strength measured at the altitude of FAST and B^{aurora} is the magnetic field strength at the ionospheric end (110 km above ground) of the flux tube that FAST is linked to, and it is obtained from the International Geophysical Reference Field (IGRF 2010). Next the precipitating electron energy flux is mapped to the auroral ionosphere at 110 km above the ground by

$$E_{\text{flux}}^{\text{aurora}} = \frac{B^{\text{aurora}}}{B^{\text{FAST}}} E_{\text{flux}}^{\text{FAST}} \tag{2}$$

Here we assume that no parallel electric fields exist between FAST and the auroral ionosphere and that the precipitating electron energy flux is conserved along a flux tube. Thus, the ratio of the energy flux at two places along the same field line equals the ratio of local magnetic field strength. At the FAST altitude, the background magnetic field is well approximated by IGRF 2010. Subtracting it from the measurements, we plot the perturbed field in Figure 1g. The red trace is the perturbed magnetic field component along the background magnetic field (i.e., pointing into the earth for the northern hemisphere), the green trace is the east-west component of the perturbed magnetic field with positive direction to the east, and the blue trace is the north-south component, positive to the north in the northern hemisphere. The FAC density plotted in Figure 1h is calculated every 0.25 s (blue trace), approximating curl-B by the change of cross-track perturbation with along-track distance, and the red trace is a 20 s running-average of the blue trace. Positive values of the current density indicate that the FAC is parallel to the background magnetic field, and vice versa. In the northern hemisphere, positive FAC is into the ionosphere, while negative FAC is out of the ionosphere. Figure 1i plots the electric field in the frame of the co-rotating plasma in the motional direction of the spacecraft (primarily north-south), obtained as

$$\mathbf{E}_{\text{NS}} = [\mathbf{E}_{\text{measured}} - (\mathbf{v}_{\text{motion}} - \mathbf{v}_{\text{coro}}) \times \mathbf{B}] \cdot \hat{\mathbf{v}}_{\text{motion}} = \mathbf{E}_{\text{measured}} \cdot \hat{\mathbf{v}}_{\text{motion}} + (\mathbf{v}_{\text{coro}} \times \mathbf{B}) \cdot \hat{\mathbf{v}}_{\text{motion}},$$

where $\mathbf{v}_{\text{coro}}$ is the velocity of ionospheric co-rotating plasmas at the FAST altitude in the Earth's inertial frame, $\hat{\mathbf{v}}_{\text{motion}} = \frac{\mathbf{v}_{\text{motion}}}{|\mathbf{v}_{\text{motion}}|}$ is the unit vector along the motional direction of FAST, and $\mathbf{E}_{\text{measured}}$ is in situ electric field measured in the spacecraft frame. A positive/negative value indicates that the electric field is parallel/antiparallel to the direction of the spacecraft motion (southward for this event). Figure 1B shows

Figure 1. (A) Data from a FAST flyby of the nightside auroral zone on 8 May 1999. Panels from top to bottom are energy flux of electrons with a pitch angle range from (a) 0°–30°, (b) 60°–120°, and (c) 150°–180°; (d) net precipitating energy flux of electrons mapped to auroral altitude at 110 km; (e) omnidirectional energy flux of ions, over an energy range from 4 eV to 25 keV; (f) energy flux of ions versus pitch angle for all energies; (g) three components of the perturbed magnetic field in a field-aligned coordinate system; (h) amplitude of the FAC density derived from magnetic field perturbations using Ampere's law with 0.25 s resolution (blue) and a 20 s running-average (red); and (i) electric field along the direction of spacecraft motion (positive southward). The blue line in Figure 1d corresponds to 0.2 erg $\text{cm}^{-2}\,\text{s}^{-1}$. The magenta rectangle in Figure 1a marks the PAA of interest. The red line in Figure 1d marks the peak of the precipitation associated with the PAA. The black lines in Figure 1g marks the boundary between the Region 1 and Region 2 FACs, and the black line in Figure 1i marks the location of the maximum eastward flow. (B) Logarithmic of the differential energy flux versus energy at 02:08:03 UT, the time that FAST encountered the peak of the precipitating electron energy flux associated with the PAA. The red line corresponds to 30% of the peak of differential energy flux. The blue dashed lines correspond to four energy bins below and above the energy bin (1379 eV) at which the differential flux peaks. (C) Plotted the same as Figure 1B but for 02:08:09 UT on the same day.

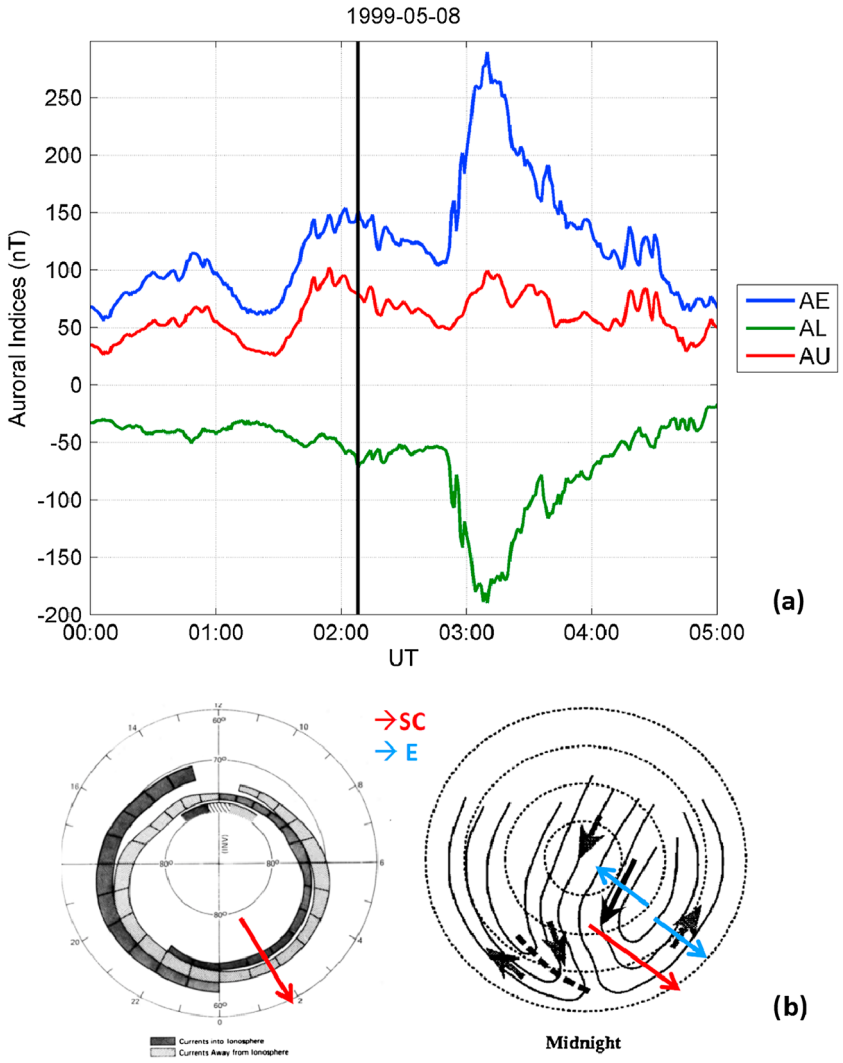

Figure 2. (a) Auroral indices from 23:00 UT on 7 May 1999 to 05:00 UT on 8 May 1999. The black line indicates the time when FAST crossed the PAA structure. (b) Ionospheric large-scale FACs (left) [*Iijima and Potemra*, 1976] and the typical substorm-growth-phase convective flow pattern in the polar cap (right) [*Koskinen and Pulkkinen*, 1995]. The dark shaded region corresponds to downward FAC into the ionosphere whereas the light shaded region corresponds to upward FAC out of the ionosphere. The red arrows indicate the FAST trajectory. The black arrows indicate flow directions, and the blue arrows indicate the direction of the convection electric field in the vicinity of FAST.

the logarithm of the differential electron energy flux versus energy at 02:08:03 UT, the time when FAST measured the peak electron precipitating flux associated with the PAA. The red dashed line indicates the 30% level of the peak precipitating energy flux, and the blue dashed lines mark the energy bins that are 50% and 200% of the energy bin at which the differential flux peaks. Figure 1c is plotted the same as Figure 1b, but for 02:08:08 UT.

Figure 2a shows the auroral indices versus UT from 2 h before to 3 h after FAST crossing of the auroral oval. The black vertical line located at 02:08 UT indicates the time FAST encountered the precipitating electron fluxes associated with the PAA. The AL index gradually decreased from −40 nT at 01:00 UT to −60 nT at 02:50 UT. At 02:50 UT, it suddenly dropped to −110 nT and later reached a minimum value of −190 nT at 03:10 UT. Thus, 02:50 UT was likely to be the substorm onset time, and accordingly, FAST crossed the PAA structure during the growth phase and ~40 min prior to the onset. Figure 2b illustrates the FAST trajectory for this event relative to a statistical average of the distribution of Region 1 and Region 2 FACs in the ionosphere [*Iijima and Potemra*, 1976] and a schematic of the convective flow in the ionosphere. In Figure 2b (left), the dark shaded regions correspond to downward FAC into the ionosphere, whereas the light shaded regions

correspond to upward FAC out of the ionosphere. The Region 1 and Region 2 FACs comprise a downward FAC sheet located adjacent to an upward FAC sheet; the pair of FAC sheets is connected by a north-south Pedersen current in the ionosphere. It has been suggested that analogously, the current system of an azimuthally extended arc is a localized double-sheet FAC structure, in which a downward FAC sheet is located adjacent to the upward FAC sheet of the arc [*Timofeev and Galperin* 1991; *Aikio et al.* 1993, and references therein]. It has also been suggested that the Pedersen current connecting the pair of FACs of the arc current system is in the same direction as the Pedersen current connecting the Region 1 and Region 2 FAC [*Timofeev and Galperin* 1991]. Therefore, for both the arc current system and the large-scale (Region 1/2) ionospheric current system, the downward FAC sheet is located equatorward of the upward FAC in the premidnight sector and poleward of the upward FAC in the postmidnight sector. We will return to this topic in section 4. In Figure 2b (right), black arrows show the schematic two-cell convective flow in the ionosphere, the red arrow indicates that in this event FAST moves across the postmidnight auroral oval from pole to equator, and the blue arrows indicate the direction of the implied convection electric field in the vicinity of FAST.

Figure 1a shows that from 02:08 UT to 02:08:05 UT, the electron energy flux is enhanced at ~1 keV, and the red color indicates that the differential energy flux at ~1 keV exceeds 10^8 (eV/eV-s-str-cm^2). In addition, the electron energy flux near 0° exceeds the flux near 180° in the same energy band. Thus, electrons with energies near 1 keV are being accelerated into the ionosphere. In Figure 1d, the precipitating energy flux associated with the increased electron precipitation from 02:08 UT to 02:08:05 UT exceeds 0.2 erg/s/cm^2. Figure 1b shows that at 02:08:03 UT, the differential energy fluxes at the energy channels 50% and 200% of the peak energy channel (1379 eV) drop below 30% of the peak energy flux. On the other hand, the energy distribution of the increased electron precipitation from 02:08:05 UT to 02:09 UT does not satisfy criterion 2(c) (Figure 1c) and thus is not qualified as monoenergetic electron acceleration. Therefore, the enhanced electron precipitation from 02:08 UT to 02:08:05 UT (marked by the magenta box) is the most equatorward monoenergetic acceleration according to our search criteria, and it is identified as the PAA. The peak of the electron energy flux associated with the PAA (marked by the red line) corresponds to the center of the PAA. In Figure 1h, the negative FAC density from 02:08 UT to 02:09:30 UT corresponds to an upward FAC sheet out of the ionosphere, whereas the positive value from 02:07:30 UT to 02:08 UT corresponds to a downward FAC sheet into the ionosphere. This is consistent with a downward Region 1 FAC sheet poleward of an upward Region 2 FAC sheet in the postmidnight sector (Figure 2b). The black vertical line in Figure 1g marks the boundary between the Region 1 and Region 2 FACs. The peak of the precipitating flux of the PAA is located very close to the interface between the Region 1 and Region 2 FAC but shifted into the upward FAC sheet. In Figure 1i, the electric field points equatorward, corresponding to eastward convective plasma flow, consistent with the illustration in Figure 2b. A sharp drop of the N-S component of the electric field is seen along the N-S direction as FAST crosses the PAA from pole to equator. This shows that eastward convective flow becomes faster poleward of the PAA. In this panel, the black vertical line marks the location of maximum southward electric field, i.e., maximum eastward flow. The PAA is located equatorward of the eastward flow maximum.

3.2. A Premidnight Event

Figure 3a shows FAST measurements made in the premidnight auroral zone near 22 MLT in the northern hemisphere on 16 June 1998, in a form analogous to that used for Figure 1. In this event, the spacecraft was moving poleward. Figure 3b shows the logarithm of the differential energy flux versus energy at 14:29:37 UT. Figure 4a shows the auroral indices 3 h before and 3 h after FAST crossed the PAA of interest (~14:30 UT), revealing that the crossing occurred during the substorm growth phase, 1 h before a sharp drop in *AL* around 15:30 UT. Figure 4b illustrates the FAST trajectory relative to the large-scale FACs and ionospheric convective flow.

In Figure 3c, electron energy flux increases in the energy range of a few keV from 14:29:30 UT to 14:29:40 UT, and the electron flux near 0° exceeds that near 180°, consistent with field-aligned acceleration of electrons into the northern hemisphere. The energy flux associated with the enhanced electron precipitation exceeds the threshold of 0.2 erg/s/cm^2 and peaks at 14:29:37 UT (marked by the red line in Figure 3d). From 14:29:30 UT to 14:29:40 UT, the differential energy flux within 50% and 200% of the peak energy channel drops below 30% of the peak energy flux (Figure 3b). Thus, the enhanced electron precipitation marked by the rectangle is the most equatorward monoenergetic precipitation according to our criteria,

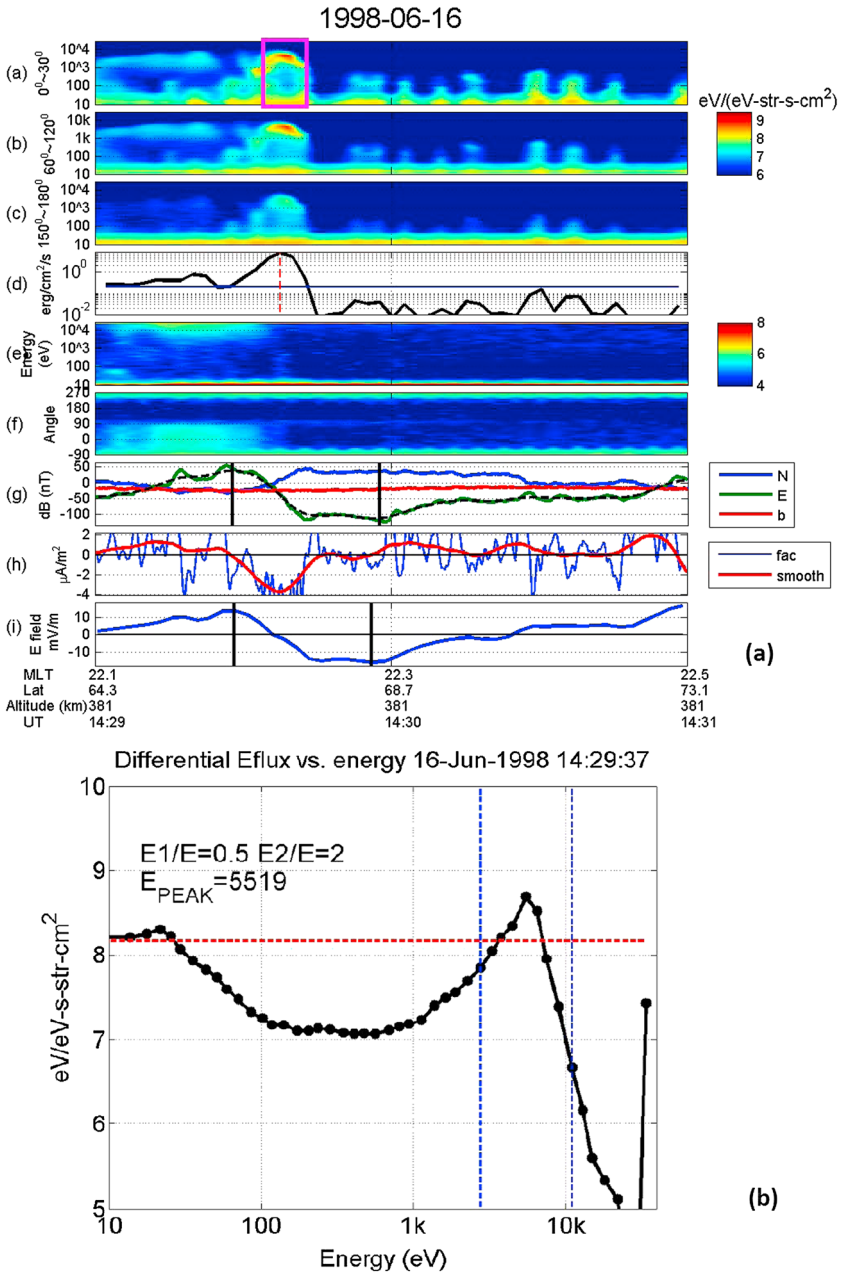

Figure 3. (A) FAST measurements from 14:29 UT to 14:31 UT on 16 June 1998. Panels from top to bottom are the same as Figure 1a. The magenta rectangle in Figure 3c marks the PAA of interest. The two vertical black lines in Figure 3i mark the maximum westward and eastward flows, respectively. (B) Differential energy flux versus energy flux at 14:29:37 UT, the time that FAST encountered the peak electron precipitation associated with the PAA in Figure 3a.

and it is identified as the PAA. The PAA is embedded within the electron plasma sheet and poleward of its inner edge. Figures 3e and 3f show that the PAA is just poleward of the enhanced energetic ion precipitation (1 keV ~20 keV) from 14:29:05 UT to 14:29:30 UT. In Figure 3h, the positive value of the FAC density corresponds to a FAC sheet parallel to the background magnetic field, i.e., into the ionosphere in the northern hemisphere, whereas the negative value corresponds to an upward FAC sheet out of the ionosphere. The polarity of the FAC is consistent with the configuration that an upward FAC sheet is sandwiched between two downward FAC sheets (Figure 4b). The black line located at the extrema of the azimuthal magnetic field in Figure 3g represents the boundaries between the Region 1 and Region 2 FACs. We find that the center of the PAA is located close to the low-latitude interface between the Region 1/2

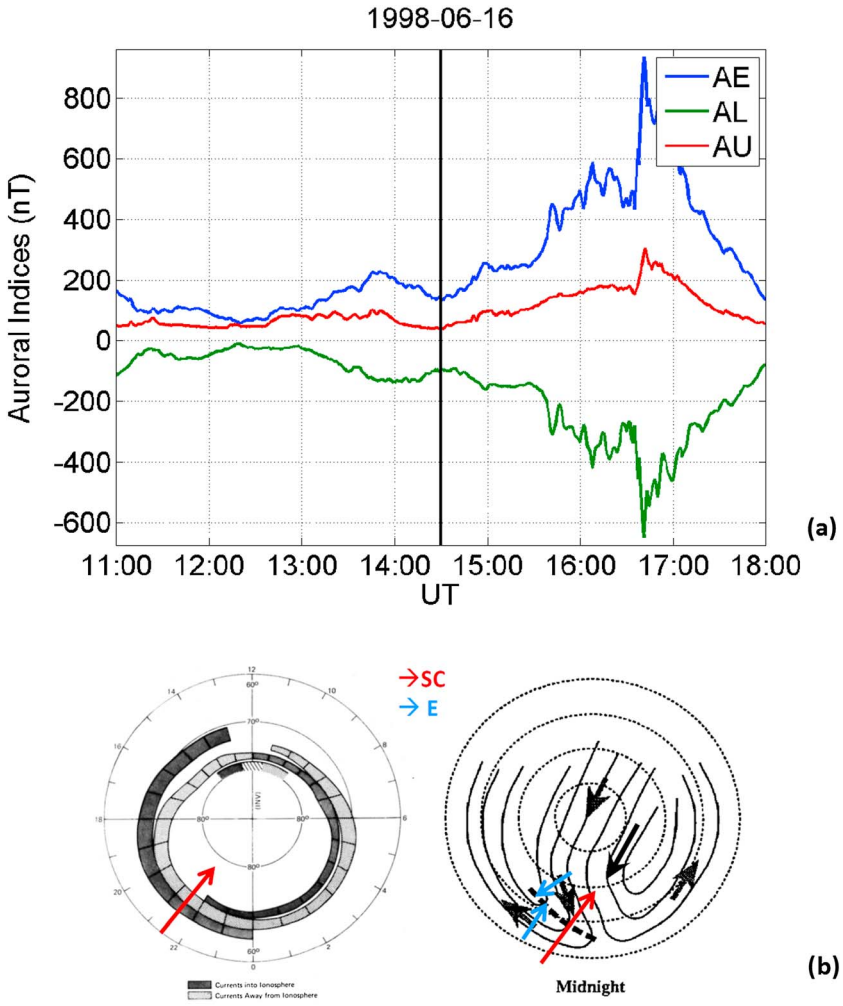

Figure 4. (a) Auroral indices from 11:00 UT to 18:00 UT on 16 June 1998. (b) FAST trajectory relative to the large-scale FACs (left) and convective flows (right) in the ionosphere for this event. FAST flew through the premidnight auroral oval from equator to pole. Arrows are colored as for Figure 2.

FAC but shifted into the upward FAC region. In Figure 3i, the poleward (positive) electric field implies westward convective flow of the plasma, while the equatorward electric field implies eastward convective flow. The PAA is located between the peak of the westward flow and the peak of the eastward flow. Since the PAA structure is located at 22 MLT, the sheared flow that rotates from east to west in the same meridian but across ~2° in latitude is likely to be the Harang flow reversal.

The two examples above show that the PAA structure identified from FAST data is located very close to the boundary between Region 1/2 FAC but slightly shifted into the upward FAC region. This is consistent with what was found for the PAAs in our previous study [*Jiang et al.*, 2012] and therefore suggests that our criteria for selecting the PAA events are robust. Furthermore, the meridional electric field in the vicinity of the PAA varies significantly along the north-south direction, corresponding to increased westward flow equatorward of the PAA in the premidnight sector and increased eastward flow poleward of the PAA in the postmidnight sector. In addition, the center of the PAA is located equatorward of the maximum eastward flow in the postmidnight sector and poleward of the maximum westward flow in the premidnight sector.

4. Statistical Results From FAST

To check whether the features identified in the cases discussed in section 3 are systematically present in the vicinity of a PAA, we carried out similar analysis for all the ~180 events identified manually from the FAST

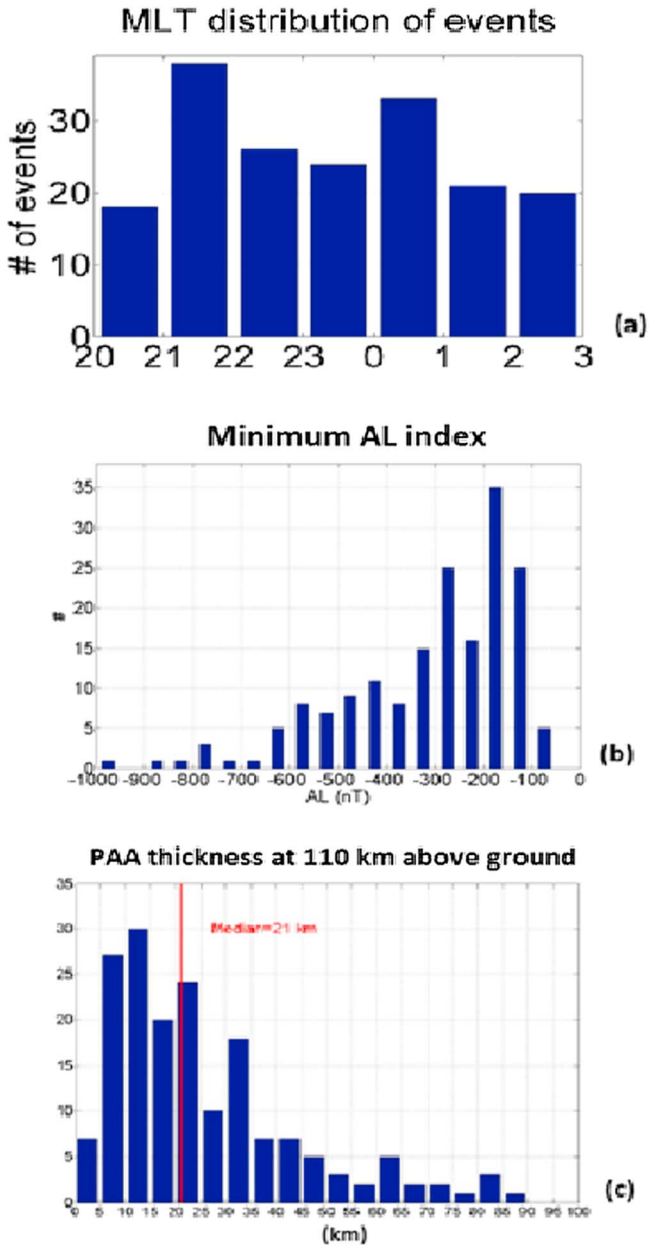

Figure 5. (a) Distribution in MLT of the PAA events. (b) Histogram of the minimum *AL* index during the substorm following FAST crossing of the PAA. (c) Distribution of PAA thickness at 110 km above ground.

data from January 1998 to June 1999. Below we present statistics of the electrodynamics associated with the preexisting arc. Figure 5a plots the local time distribution of the PAA events identified from the FAST data. It shows that the FAST events are roughly evenly distributed in MLT between 20 and 3. Figure 5b plots the distribution of the minimum *AL* index during the substorm following the FAST crossing of the PAA. The median *AL* is −275 nT, suggesting that the substorms examined in this data set are strong enough to cause a global magnetic disturbance.

Figure 5c shows the distribution of the latitudinal width of the PAA at 110 km above ground. The low-latitude and high-latitude edges of the PAA are identified as the boundary of the electron precipitation associated with the PAA where the energy spectra transition from monoenergetic to diffuse or broadband, based on criteria 2. The latitudinal separation at FAST altitude is then mapped to auroral altitude to obtain arc width. The distribution shows that majority widths of the PAA (~80%) lie within 50 km and the median width is ~21 km. This is consistent with the thickness of the growth-phase arc obtained from all-sky imager observations by *Nishimura et al.* [2011] (Figure 7) and shows that our criteria are robust in extracting the latitudinally thin PAAs.

4.1. Location of the PAA Relative to Energetic Ion Precipitation

Figure 6 plots the median (solid traces) and quartiles (dashed traces) of precipitating ion energy flux integrated over the energy range between 1 keV and 25 keV from 2° equatorward of the center of the PAA to 2° poleward of the center of the PAA, for premidnight (left) and postmidnight (right) events, respectively. The center of the PAA corresponds to the peak of the electron precipitation associated with the PAA and is marked by the red line. For the premidnight events, the PAA is found to be embedded within the increased ion precipitation but ~1° poleward of the peak precipitating flux. This is quite consistent with optical observations of the PAA in many previous studies [e.g. *Samson et al.*, 1992; *Lessard et al.*, 2007] and indicates that our event selection is robust. For the postmidnight events, the PAA is found to be very close to the peak of the energetic ion precipitation. This is due to the difference in the ion and electron drift paths in the magnetosphere. The electrons drift closer to the earth on the dawnside than on the duskside. The ion drift paths are more complicated compared with the electrons—cold ions follow the drift path of electrons more or less, while hot ions drift closer to the earth on the duskside than on the dawnside. Medium energy ions

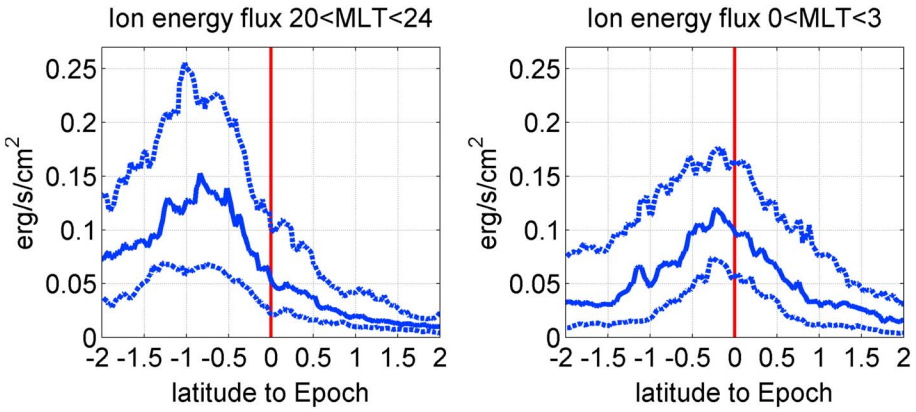

Figure 6. Precipitating ion energy flux integrated from 1 keV to 25 keV from 2° equatorward to 2° poleward of the center of PAA for premidnight passes and postmidnight passes, respectively. Zero corresponds to latitude of the peak electron precipitation associated with the PAA. The solid traces are medians, and the dashed traces are quartiles.

can penetrate deep into the magnetosphere on the duskside (nose ions). A statistical study by *Zou et al.* [2012] revealed that at quiet times, dusk-premidnight proton aurora extends slightly equatorward of the electron aurora and that in the postmidnight sector, electron aurora extends equatorward of the proton aurora. As a result, the latitudinal separation between the PAA and the peak ion energy flux is closer in the postmidnight sector than in the premidnight sector.

4.2. Location of the PAA Relative to Large-Scale FACs and Convective Flows

In this section, the relationship between the location of the PAA and the Region 1/2 FAC boundary is investigated. As for the events shown in Figures 1 and 3, the center of the PAA is identified from the net precipitating electron energy flux, while the boundary between the Region 1/2 FACs is identified from the curl of the azimuthal component of the perturbed magnetic field. Figure 7a displays a histogram of the latitude of the PAA relative to that of the Region 1/2 FAC boundary, i. e., $d\lambda = |\lambda_{PAA}| - |\lambda_{R1R2}|$, where $|\lambda_{PAA}|$ is the absolute value of the invariant latitude of the PAA and $|\lambda_{R1R2}|$ is the absolute value of the invariant latitude of the Region 1/2 FAC boundary. With $d\lambda = 0$ defined as the Region 1/2 FAC boundary, a positive (negative) $d\lambda$ implies that the PAA is poleward (equatorward) of the Region 1/2 FAC boundary in either hemisphere. Figure 7a (left) is for passes in the premidnight sector between 20 MLT and 24 MLT. For most (~65%) of the events in this region, the center of the PAA is located within 1° poleward of the Region 1/2 FAC boundary, embedded within the upward Region 1 FAC. A significant peak (45% of all premidnight events) is seen where the center of the PAA is located within 0.5° poleward of the Region 1/2 FAC boundary. Figure 7a (right) shows that for most (~60%) of the passes in the postmidnight sector between 00 MLT and 03 MLT, the center of the PAA is located within 1° equatorward of the Region 1/2 FAC boundary, embedded within the upward Region 2 FAC. Considering that the width of the PAA is usually a fraction of one degree (~100 km), this statistical study confirms the finding that the arc structure is located very close to the boundary between the Region 1 and Region 2 FAC and slightly shifted into the upward FAC. It shows that our criteria for identifying the PAA structure are robust.

Figure 7b plots the distribution of latitudinal separation between the PAA and the R1/R2 boundary in the same format as Figure 7a, but for passes between 22 MLT and 01 MLT in which three FAC sheets are present. Figure 7a (left) shows the latitudinal separation between the PAA and the low-latitude R1/R2 boundary, while Figure 7a (right) shows that between the PAA and the high-latitude R1/R2 boundary. Our statistics indicate that 80% of the PAAs are located in the upward FAC region sandwiched between the two downward FAC sheets and that 50% of the PAAs are located within 0.5° poleward of the low-latitude R1/R2 boundary. Therefore, in the midnight region where three FAC sheets are present, the most likely location of the PAA lies slightly poleward of the low-latitude R1/R2 boundary.

In addition to linking the locations of the PAA to the Region 1/2 FAC boundary, we have also benchmarked the PAA's location relative to large-scale convective flows. In a typical growth phase, the ionospheric flow

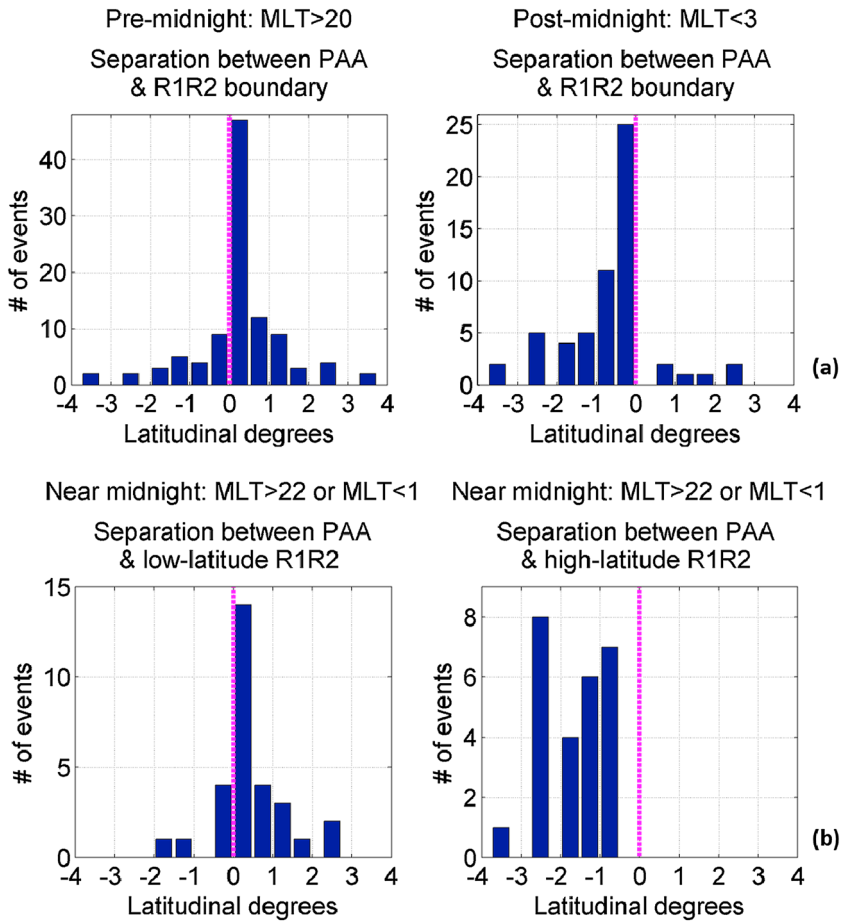

Figure 7. (a) Histogram of the invariant latitude of the PAA relative to that of the Region 1/2 FACs boundary ($x = 0$, marked in magenta) in the premidnight and postmidnight sectors, i.e., $d\lambda = |\lambda_{PAA}| - |\lambda_{R1R2}|$, where $|\lambda_{PAA}|$ and $|\lambda_{R1R2}|$ are the absolute values of the invariant magnetic latitudes of the PAA and the Region 1/2 FAC boundary, respectively. Figure 7a (left) is for postmidnight passes, while Figure 7a (right) is for premidnight passes. (b) The same as Figure 7a but for PAAs events between 22 MLT and 01 MLT and for which three FAC sheets are identified.

has a two-cell convection pattern, in which plasmas are transported from the dayside to the nightside at high latitudes and returned to the dayside at lower latitudes. We identify azimuthal flow maxima from electric field measurements and display the histogram of the latitude of the PAA relative to the azimuthal flow peak in Figure 8a. The events in which FAST observed sharp bipolar electric field signatures and upward-going ion beams with an energy from a few hundred eV to a few keV have been excluded, as these are signatures of the acceleration region in which the bipolar electric field are produced by a U-shaped potential drop and the electric fields do not map to ionospheric convective flows. The latitudinal separation is calculated as $d\lambda = |\lambda_{PAA}| - |\lambda_{flow\_peak}|$, where $|\lambda_{PAA}|$ and $|\lambda_{flow\_peak}|$ are the absolute values of the invariant latitude of the PAA and the azimuthal flow peak, respectively. $d\lambda = 0$ is defined as the invariant latitude of the maximum azimuthal flow. Figure 8a (left) is for passes in the premidnight sector, while Figure 8a (right) is for passes in the postmidnight sector. In the morning sector, the PAA is mostly located equatorward of the maximum eastward flow. In the evening sector, however, the PAA lies poleward of the maximum westward flow as often as it lies equatorward of the maximum westward flow. The presence of the Harang discontinuity and associated distortions of flow boundaries in the premidnight region may account for the spread of the distribution. The Harang discontinuity spans a range of local times within which the eastward electrojet lies equatorward of the westward electrojet [*Harang*, 1946; *Heppner*, 1972], usually appearing as clockwise rotation of flow vectors from eastward flow at higher latitudes to westward at lower latitudes. This distorted flow pattern may produce a latitudinal spread of the westward flow peak. As a result, the location of the PAA relative to the westward flow peak is less well organized in the evening than in the morning sector.

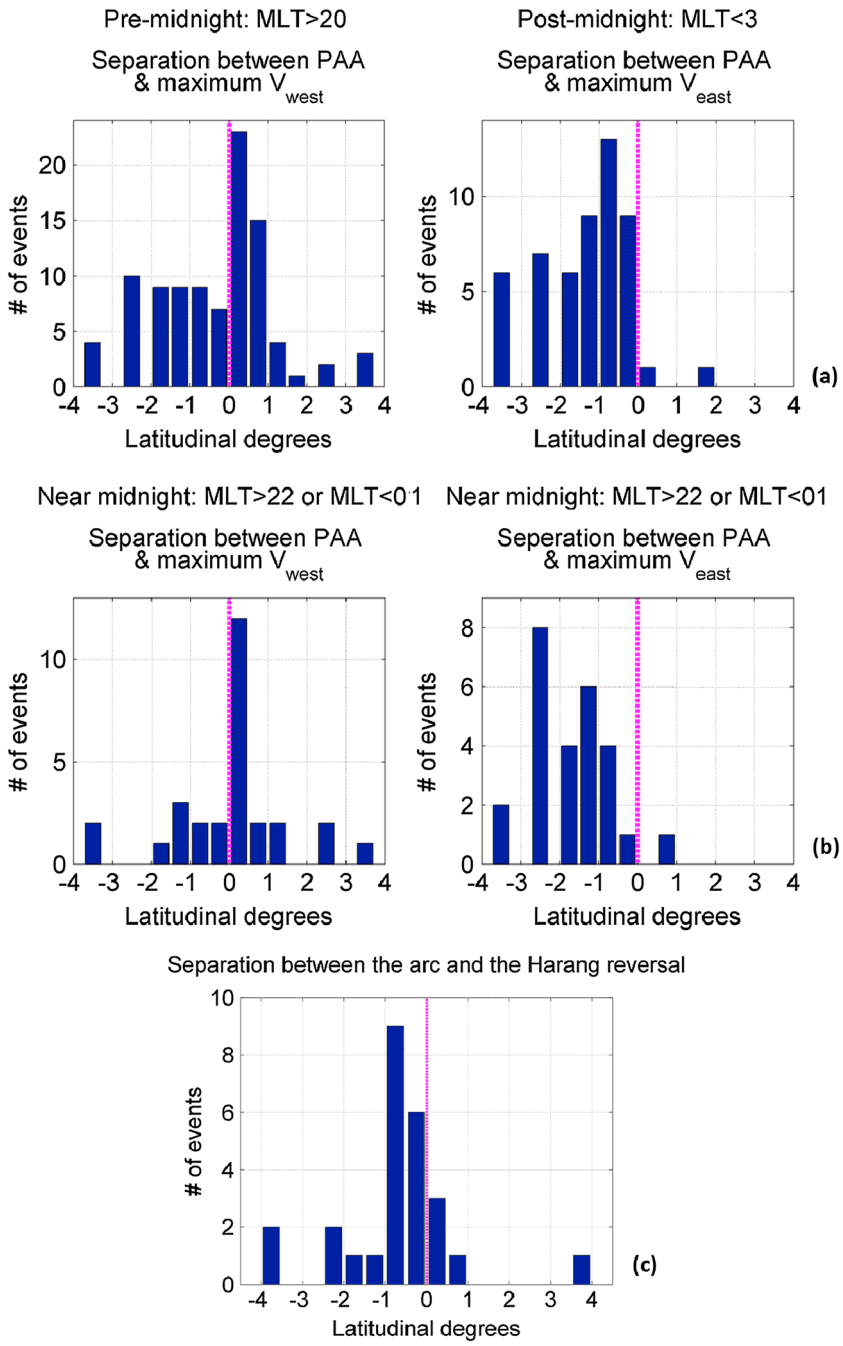

Figure 8. (a) Histogram of the invariant latitude of the PAA relative to that of the maximum azimuthal return flow ($x = 0$, marked in magenta), i.e., $d\lambda = |\lambda_{PAA}| - |\lambda_{flow\_peak}|$, where $|\lambda_{PAA}|$ and $|\lambda_{flow\_peak}|$ are the absolute values of the invariant magnetic latitudes of the PAA and the azimuthal flow peak, respectively. Figure 8 (left) is for postmidnight passes, while Figure 8 (right) is for premidnight passes. (b) Histogram of the invariant latitude of the PAA relative to that of the maximum azimuthal flow for events between 22 MLT and 01 MLT and for which three FAC sheets are identified. Marked in magenta, $x = 0$ is defined as the invariant latitude of the maximum azimuthal flow. (c) Histogram of the invariant latitude of the PAA relative to the flow reversal point, i.e., $d\lambda = |\lambda_{PAA}| - |\lambda_{V=0}|$. The flow reversal point is taken to lie between the westward flow peak and the eastward flow peak where the azimuthal flow speed becomes zero.

The relationship between the location of the substorm breakup arc and that of the Harang reversal has been studied by various authors [*Nielsen and Greenwald*, 1979; *Baumjohann* et al., 1981; *Gjerloev et al.*, 2003; *Zou et al.*, 2009], and it is of interest to compare our results with previous studies. In Figures 8b and 8c, we select passes in the local time range between 22 MLT and 01 MLT in which three FAC sheets are present

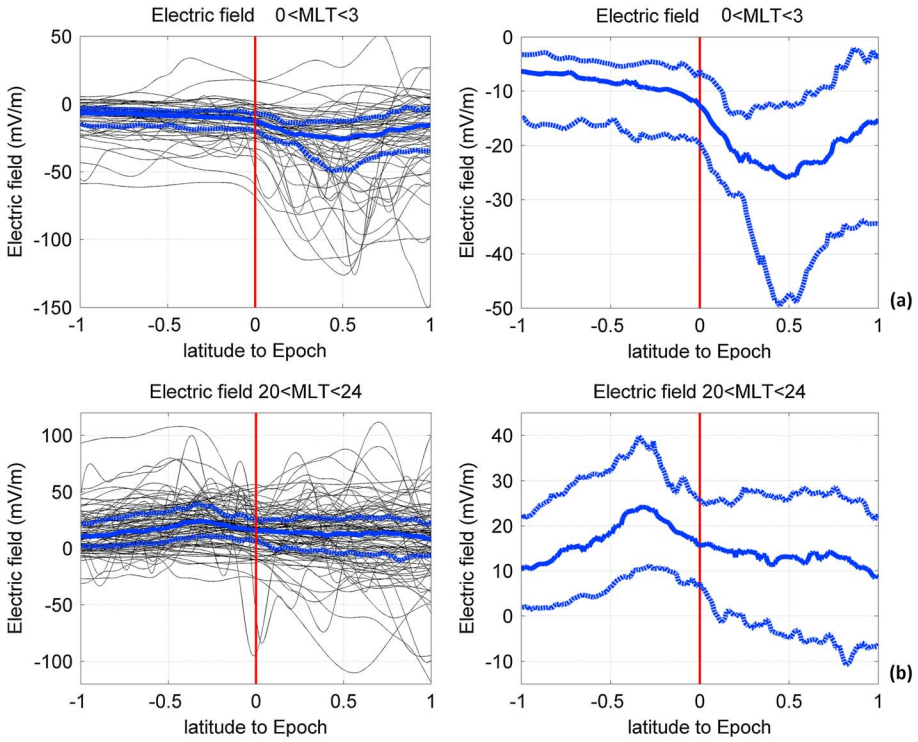

Figure 9. Electric field along the FAST trajectory versus the invariant latitude of FAST relative to the invariant latitude of the PAA ($x = 0$, marked in red) for (a) postmidnight passes and (b) premidnight passes. Positive is in the poleward direction. Individual profiles of the electric field from equator to pole (black traces), the median (solid blue trace), and the quartiles (dashed blue traces) are plotted. Figures 9a and 9 b (right) are for a smaller range of electric field intensities than panels on the left so that the quartiles can be seen more clearly.

and plot the PAA's location relative to the azimuthal flow peak as well as the flow reversal point. It is worth noting that the electric field probes on FAST are in the spin-plane and measure only the north-south and field-aligned components. Therefore, the electric field data here enable one to identify azimuthal flows but not north-south flows, and one needs to bear this in mind when looking at the flow distribution. Figure 8b plots the histogram of the latitude of the PAA relative to those of the maximum westward and eastward flows, respectively. It shows that near midnight, the PAA is predominantly located between the eastward flow peak and the westward flow peak. Figure 8c plots the histogram of the latitudinal separation between the PAA and the flow reversal point, which is identified as the point between the westward flow peak and the eastward flow peak at which the azimuthal flow speed becomes zero. The histogram implies that majority of the PAAs (~80%) lie equatorward of the flow reversal point in the presumed Harang region. This result is most consistent with that of *Baumjohann et al.* [1981] in which they found that substorm breakup arcs occurred slightly equatorward of the Harang flow reversal and in the region of northwestward directed electric fields.

4.3. Flow Pattern Associated With the PAA

In the two cases described in section 3, there is a shear in the azimuthal flow across the PAA; i.e., westward flows increase equatorward of the PAA in the premidnight sector and eastward flows increase poleward of the PAA in the postmidnight sector. To establish whether this type of flow structure is typical for all the cases examined, we superimpose the north-south electric field along the FAST path from 1° equatorward of the center of PAA to 1° poleward in Figure 9. Figure 9a is for postmidnight passes, while Figure 9b is for premidnight passes. The epoch zero, marked by the red line, is the invariant latitude of the peak electron energy fluxes of the PAA, as illustrated in Figures 1d and 3d. The events in which FAST observed sharp bipolar electric field signatures and upward-going ion beams with an energy from a few hundred eV to a few keV have been excluded, as these are signatures of the acceleration region in which the bipolar electric field are produced by a U-shaped potential drop and do not map to the bottom of the ionosphere.

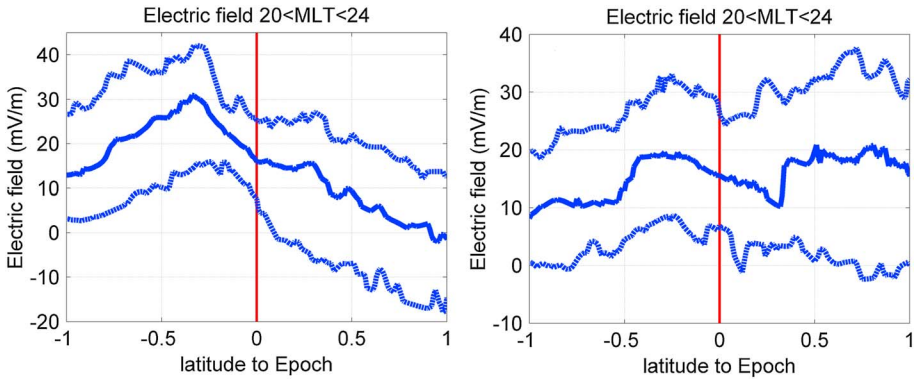

Figure 10. Electric field along the FAST trajectory versus the invariant latitude of FAST relative to the invariant latitude of the PAA ($x = 0$, marked in red) in the premidnight sector: (left) for the subset of cases where the PAA is located poleward of the peak of the poleward electric field and (right) for the remaining cases where the PAA is located equatorward of the peak of the poleward electric field. The solid traces are the medians, and the dashed traces are the quartiles of the data.

For each pass not excluded by having a sharp bipolar signature, the electric field in the plasma co-rotating frame has been mapped along field lines (assumed to be equipotentials) to a common altitude at 110 km above the surface of the Earth. Additionally, we have excluded events where the electric field at 110 km above ground exceeds 150 mV/m, as this magnitude is rarely observed in the auroral ionosphere. In Figure 9, the x axis is the invariant latitude of FAST relative to that of the PAA. The black traces in Figure 9 represent individual electric field profiles as FAST moves from equator to pole. Since a positive electric field is along the motional direction of FAST (equator to pole), and the convection electric field is equatorward in the postmidnight sector, the black traces in Figure 9a are mostly in the negative range. The solid blue curve is the median of the black traces, and the dashed blue curves are the lower and upper quartiles. The variation of the median and quartiles across the arc is more evident in Figures 9a and 9b (right). On average, the electric field remains relatively constant at around 5–10 mV/m equatorward of the PAA and then drops to −25 mV/m ~0.5° poleward of the PAA. Although there are large fluctuations, the trend is also evident for the individual passes.

In the premidnight region (Figure 9b), the convection electric field associated with the return flow is poleward, so the black traces are mostly in the positive range. Consistent with the second case in section 3, the median of the electric field increases equatorward of the PAA. Although scatter of the data is considerable, the plot over a large range of electric field intensities (Figure 9b, left) makes clear that the trend shown by the median and the quartiles is meaningful. Evidently $\partial E_x/\partial x$ (x is along the north-south direction) in the premidnight sector is less pronounced than that in the postmidnight sector, and a plateau develops poleward of epoch zero. The plateau probably results from the complex distribution of large-scale flows in the premidnight sector. Figure 7 indicates that for almost half of the cases in the premidnight sector, the maximum electric field is located poleward of the PAA. As a result, $\partial E_x/\partial x$ across the PAA is smaller in this sector than that in the postmidnight sector. To illustrate this point, Figure 10 plots the median and quartiles of the electric field across the PAA in the premidnight sector for the subset of cases where the PAA is located poleward of the maximum electric field (left) and for the remaining cases where the PAA is located equatorward of the maximum electric field (right). The pattern in Figure 10 (left) is consistent with the model of increased flow centered just equatorward of the arc in the premidnight sector, except that $\partial E_x/\partial x$ is larger compared with Figure 9b. In Figure 10 (right), the electric field starts to increase with latitude ~0.25° poleward of epoch, and the overall variation of the electric field over 2° across the PAA is less pronounced than that in Figure 10 (left). Nevertheless, a localized drop of the N-S component of the electric field in the N-S direction, corresponding to a flow shear, is present across the center of the PAA (from −0.3° to 0.25°). Figure 10 shows that in the premidnight sector, increased westward flow is present in the equatorward vicinity of the PAA, and the spatial scale and magnitude of the flow shear is dependent on the arc's location relative to the peak of the westward flow.

4.4. Electrodynamics of the PAA

In order to understand why the electric field increases adjacent to the PAA, we consider equations that describe arc-associated electrodynamics. In the ionosphere, the current perpendicular to the background magnetic field can be broken into the Pedersen current and the Hall current, i. e.,

$$\mathbf{j}_\perp = \sigma_p \mathbf{E} + \sigma_H \hat{\mathbf{b}} \times \mathbf{E} \tag{3}$$

where σ_P and σ_H are the Pedersen and Hall conductivities, respectively, $\mathbf{E}$ is the electric field, and $\hat{\mathbf{b}}$ is a unit vector along the background magnetic field. Integrating equation (3) along the field line and assuming that the field-aligned direction and the electric field vary little with the ionospheric height at the auroral altitudes, we get

$$\mathbf{J}_\perp = \Sigma_p \mathbf{E} + \Sigma_H \hat{\mathbf{b}} \times \mathbf{E} \tag{4}$$

Here Σ_P and Σ_H are the height-integrated Pedersen and Hall conductivities, respectively, and $\mathbf{J}_\perp$ is the height-integrated current density. For steady state, the current density is divergence free, i.e.,

$$\nabla_\perp \cdot \mathbf{j}_\perp + \frac{\partial \mathbf{j}_z}{\partial z} = 0 \tag{5}$$

Integrating equation (5) along the field-aligned direction, one finds

$$\nabla_\perp \cdot \mathbf{J}_\perp = -\left(j_z^{\text{top}} - j_z^{\text{bot}}\right) = -j_z^{\text{top}} \tag{6}$$

Here we recognize that no currents flow out of the bottom of the ionosphere ($j_z^{\text{bot}} = 0$). Replacing $\mathbf{J}_\perp$ with equation (4), the field-aligned current density can be expressed as

$$j_z = -\nabla_\perp \cdot \left(\Sigma_p \mathbf{E} + \Sigma_H \widehat{\mathbf{b}} \times \mathbf{E}\right) \tag{7}$$

Expanding equation (7) in a Cartesian coordinate where the x axis points poleward, y axis points to the east, and z axis points along the background magnetic field, one gets

$$-j_z = \frac{\partial(\Sigma_p E_x)}{\partial x} - \frac{\partial(\Sigma_H E_y)}{\partial x} + \frac{\partial(\Sigma_p E_y)}{\partial y} + \frac{\partial(\Sigma_H E_x)}{\partial y} \tag{8}$$

For a quasi-steady PAA, the variation in the azimuthal direction is in general much smaller than the variation in the meridional direction, i. e., $\frac{\partial}{\partial y} << \frac{\partial}{\partial x}$. If the convective flow is mainly in the azimuthal direction and the dominant component of the electric field is north-south, i.e. $E_x >> E_y$, equation (8) is well approximated by

$$-j_z = \frac{\partial(\Sigma_p E_x)}{\partial x} \tag{9}$$

Equation (9) shows that the FAC density depends on how E_x and Σ_p vary with latitude, given the assumption that the variation in the azimuthal direction is much smaller than the variation in the meridional direction. Figure 11 shows profiles of various quantities across the PAA in the postmidnight sector and in the premidnight sector, respectively. The values are plotted against magnetic latitude relative to epoch, which is defined as the invariant latitude of the peak electron energy flux of the PAA. Panels from top to bottom are electric field along the FAST trajectory (same as Figure 9), height-integrated Pedersen conductivity Σ_p, and FAC density derived from equation (9) (blue) and from the perturbed magnetic field (black), both of which are smoothed by a 6 s running-average window. In Figure 11, the solid blue traces are the medians while the dashed blue traces are quartiles of the data. The height-integrated Pedersen conductance is estimated using the formula in *Robinson et al.* [1987] and *Galand and Richmond* [2001], where the contribution to the Pedersen conductance from proton precipitation is $\Sigma_P^+ = 5.7 Q_+^{0.5}$ and the contribution to the Pedersen conductance from electron precipitation is $\Sigma_P^- = \frac{40<W>}{16+<W>^2} Q_-^{0.5}$. Here Q_- and Q_+ are the precipitating energy fluxes at 110 km

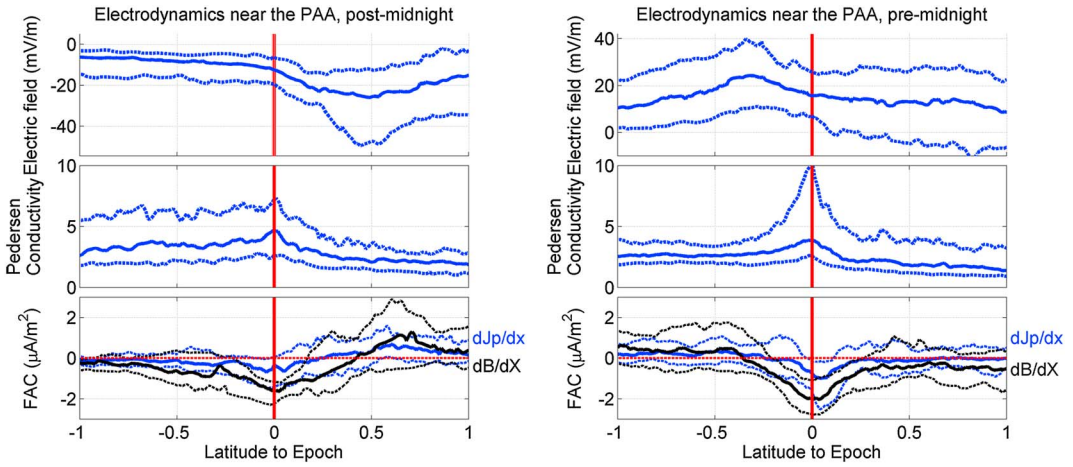

Figure 11. Profiles of various quantities from −1° equatorward of the center of the PAA to 1° poleward of the PAA for (left) postmidnight passes and (right) premidnight passes, respectively. Panels from top to bottom are the electric field along FAST trajectory (positive in the poleward direction); height-integrated Pedersen conductivity, evaluated as explained in the text; and FAC density inferred magnetic field perturbations (black) and FAC density inferred from equation (9) (blue). Epoch zero (marked by the red line) corresponds to the center of the preexisting arc inferred from precipitating electron energy fluxes. The solid traces are the medians and the dashed traces are the quartiles.

above ground for electrons and protons, respectively, and they are calculated from equations (1) and (2); $<W>$ is the mean energy of the incident particles in keV. The total Pedersen conductance is $\Sigma_P = \sqrt{\left(\Sigma_P^-\right)^2 + \left(\Sigma_P^+\right)^2}$ [*Galand and Richmond*, 2001]. In the third panel, negative values correspond to upward FAC while positive values correspond to downward FAC.

In the third panels of Figure 11, the FAC density inferred from equation (9) is qualitatively consistent with the FAC density inferred from the magnetic perturbations. In the postmidnight sector (Figure 11, left), an upward FAC current sheet is located equatorward of a downward FAC sheet, whereas in the premidnight sector (Figure 11, right), an upward FAC is located poleward of a downward FAC sheet. The upward FAC density peaks near the center of the PAA. Overall, the FAC density calculated from equation (9) mimics the trend of the FAC density inferred from magnetic perturbations fairly well, and the boundary between the upward and the downward FACs inferred from two approaches are located close together. However, the FAC density inferred from the divergence of the Pedersen current is less than 50% of that inferred from the magnetic perturbations. To further investigate current structure in the vicinity of the PAA, we plot in Figure 12 the medians of the azimuthal (B_y) and north-south (B_x) magnetic perturbation from −10° equatorward of epoch (peak of the precipitating electron fluxes associated with the PAA) to 14° poleward of epoch, at different local time sectors.

Figure 12 shows that in the vicinity of the PAA, variation in B_y (40~50 nT/degree) is much larger than the variation in B_x (~30 nT across ~2 MLT or ~1 nT/degree). This indicates that the PAA is an azimuthally extended field-aligned current sheet. Additionally, the net B_y change in the vicinity of the PAA is close to 0 in all local time sectors, suggesting that the intensity of the upward FAC nearly balances the intensity of the downward FAC. This implies that the ionospheric closure current of the PAA is dominantly north-south Pedersen current, because if the FAC of the PAA were closed by east-west Pedersen current, there would be no reason to expect near balance in the intensity of the upward and downward FACs, as they would be independent current system in this case. Furthermore, if the FACs were closed by east-west Pedersen currents, there would be an east-west gradient in the FAC density, and this would manifest as a signature in the north-south component of the magnetic field. However, the statistics here as well as the examples in Figures 1 and 3 show that variation in B_x is much smaller than variation in B_y. Therefore, the data presented in this work are consistent with north-south Pedersen current as the dominant closure current of the PAA.

Figures 11 and 12 favor the north-south Pedersen current as the ionospheric closure current of the PAA. The Pedersen current provides the $j \times B$ force that couples ionospheric plasmas to the magnetospheric flows.

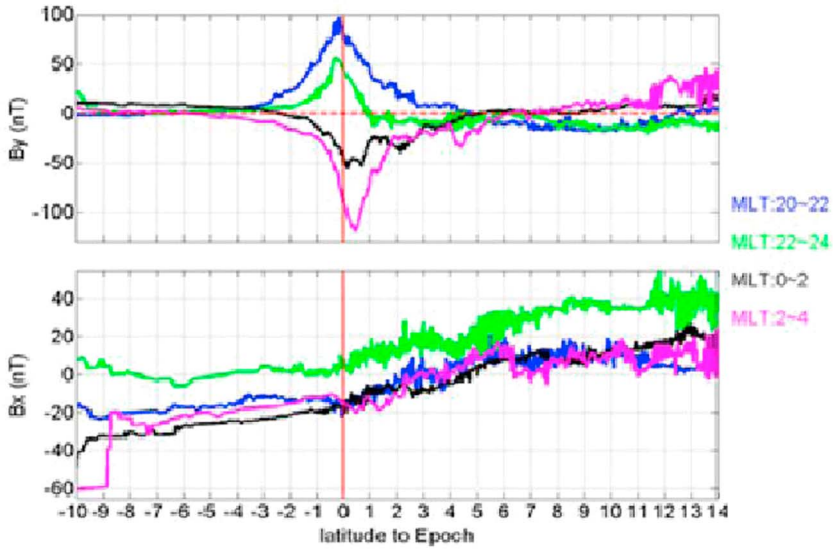

Figure 12. Medians of the B_y and the B_x components of the magnetic perturbation from −10° equatorward of epoch to 14° poleward of epoch. Different colors represent different local time sectors.

Premidnight, the $j_P \times B$ force moves the plasmas westward, whereas postmidnight, the $j_P \times B$ force moves the plasmas eastward. We speculate that the discrepancy between the FAC density inferred from magnetic perturbations and that calculated from equation (9) in Figure 11 arises from underestimation of the ionospheric conductance, due to the underestimation of the precipitating fluxes, as the discrepancy in the upward FAC region is larger than the discrepancy in the downward FAC region.

With the guidance of equations (3)–(9), the enhancement of the N-S electric field adjacent to the PAA can be understood intuitively as follows. In the ionosphere, the current system of the PAA consists of an upward FAC sheet, a downward return FAC sheet adjacent to the arc, and a meridional Pedersen current that connects the pair of FACs. In the downward return FAC region, ionospheric conductivity is low because of the outflow of cold ionospheric electrons carrying the current [*Doe et al.* 1995; *Karlsson and Marklund,* 1996]. In the upward FAC region, conductivity is relatively high because of the increased electron precipitation. In order to maintain continuity of the N-S Pedersen current across the arc, the electric field in the low conductivity region (downward FAC) needs to increase. In the premidnight sector, the downward FAC sheet is located equatorward of the upward FAC sheet, whereas in the postmidnight sector, the downward FAC sheet is located poleward of the upward FAC. Consequently, an increased electric field is observed equatorward of the PAA in the premidnight sector and poleward of the PAA in the postmidnight sector.

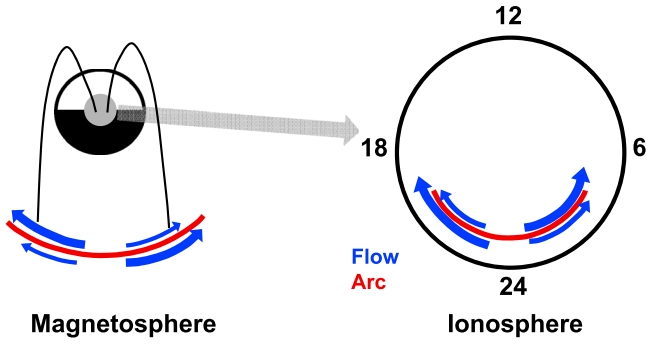

Figure 13. Schematic flow pattern near the preexisting arc in the ionosphere and on the equatorial plane in the magnetosphere. The red curve represents the preexisting arc. Blue arrows represent accelerated flow channels adjacent to the arc or its source in the magnetosphere.

5. Conclusions

In the work presented here, we characterized the statistical pattern of ionospheric flows and FACs associated with a PAA. Conclusions of this work are as follows:

1. In the premidnight region, the PAA is typically located within 1° poleward of the R1/R2 boundary (65%). In the postmidnight region, the PAA is typically located within 1° equatorward of the R1/R2 boundary (60%). Therefore, the most probable arc location is near the R1/R2 boundary but displaced into the region carrying upward FAC from the ionosphere.
2. In the postmidnight sector, the majority of the arcs lie equatorward of the maximum eastward flow. In the premidnight sector, the PAA is found within 3° of the maximum westward flow, sometimes equatorward and sometimes poleward. A large fraction (40%) of the PAAs are located within 1° poleward of the westward flow peak.
3. Near midnight where three FAC sheets are present, most of the PAAs (70%) are located in the upward FAC region. Fifty percent of the PAAs lie 0.5° poleward of the low-latitude R1/R2 boundary. Additionally, the PAA is typically located between the maximum westward and eastward flow, and equatorward of the flow reversal point (zero azimuthal flow). Many of the anomalous cases in the premidnight region appear to reflect the complex flow patterns in the Harang region.
4. FAST statistics indicate that in the premidnight sector, a downward FAC sheet is located equatorward of and adjacent to the upward FAC sheet of the, PAA while in the postmidnight sector, a downward FAC sheet is located poleward of the upward FAC of the PAA. Comparison of the FAC density inferred from the divergence of the N-S Pedersen current and that from magnetic perturbations, as well as comparison between the meridional and the azimuthal components of the magnetic perturbation, favors the view that the FAC associated with the PAA is mainly closed by N-S Pedersen current in the ionosphere.
5. In the ionosphere, the eastward flow speed increases over 0.5° poleward of the PAA in the morning sector whereas the westward flow speed increases over 0.5° equatorward of the PAA in the evening sector. The average speed of the azimuthal flow adjacent to the arc is ~1 km/s, which corresponds to an azimuthal flow of 60~80 km/s in the magnetotail where the magnetic field is a few nanotesla (assuming that field-aligned potential drop is small compared with the cross field line potential drop).

The ionospheric flow shear associated with the PAA has been observed for general discrete arcs during quiescent times [e.g., *Marklund*, 1984; *Timofeev and Galperin*, 1991]. On the other hand, compared with the wide spread of discrete auroral arcs in the Region 1/2 currents [*Ohtani et al.*, 2010], the confined location of the PAA relative to large-scale ionospheric convection and FACs is a unique feature of the PAA itself. The arc-associated flow shear observed from FAST suggests that the corresponding flow pattern in the magnetosphere should be increased duskward flow earthward of the source region of the PAA in the evening sector and increased dawnward flow tailward of the source region of the PAA in the morning sector (Figure 13). Whether such a flow shear is present in the magnetosphere will be addressed in a subsequent study.

Acknowledgments

This work was supported by the NASA THEMIS funding 443869-TM-22620. R.J.W. would like to acknowledge the Independent Research and Development support from NSF. Helpful discussion with Jun Liang is greatly appreciated. We are grateful to valuable feedback from Octav Marghitu on our work.

Michael Balikhin thanks Octav Marghitu, Kristina Lynch, and Goran Marklund for their assistance in evaluating this paper.

References

Aikio, A. T., H. J. Opgenoorth, M. A. L. Persson, and K. U. Kaila (1993), Ground-based measurements of an arc-associated electric field, *J. Atmos. Terr. Phys.*, *55*(4–5), 797–808, doi:10.1016/0021-9169(93)90021-P.

Akasofu, S. I. (1964), The development of the auroral substorm, *Planet. Space Sci.*, *12*(4), 273–282.

Baumjohann, W., R. J. Pellinen, H. J. Opgenoorth, and E. Nielsen (1981), Joint two-dimensional observations of ground magnetic and ionospheric electric fields associated with auroral zone currents: Current systems associated with local auroral breakup, *Planet. Space Sci.*, *29*, 431–447, doi:10.1016/0032-0633(81)90087-8.

Brüning, K., C. K. Goertz, and K. Wilhelm (1985), Why does the perpendicular electric field increase at the edge of auroral arcs?, *Adv. Space Res.*, *5*(4), 79–82, doi:10.1016/0273-1177(85)90119-X.

de la Beaujardière, O., R. Vondrak, and M. Baron (1977), Radar observations of electric fields and currents associated with auroral arcs, *J. Geophys. Res.*, *82*(32), 5051–5062, doi:10.1029/JA082i032p05051.

de la Beaujardière, O., R. Vondrak, R. Heelis, W. Hanson, and R. Hoffman (1981), Auroral arc electrodynamic parameters measured by AE-C and the Chatanika Radar, *J. Geophys. Res.*, *86*(A6), 4671–4685, doi:10.1029/JA086iA06p04671.

Doe, R. A., J. F. Vickrey, and M. Mendillo (1995), Electrodynamic model for the formation of auroral ionospheric cavities, *J. Geophys. Res.*, *100*(A6), 9683–9696, doi:10.1029/95JA00001.

Galand, M., and A. D. Richmond (2001), Ionospheric electrical conductances produced by auroral proton precipitation, *J. Geophys. Res.*, *106*(A1), 117–125, doi:10.1029/1999JA002001.

Gjerloev, J. W., R. A. Hoffman, E. Tanskanen, M. Friel, L. A. Frank, and J. B. Sigwarth (2003), Auroral electrojet configuration during substorm growth phase, *Geophys. Res. Lett.*, *30*(18), 1927, doi:10.1029/2003GL017851.

Harang, L. (1946), The mean field of disturbance of polar geomagnetic storms, *Terr. Magn. Atmos. Electr.*, *51*(3), 353–380, doi:10.1029/TE051i003p00353.

Harvey, P. R., D. W. Curtis, H. D. Heetderks, D. Pankow, J. M. Rauch-Leiba, S. K. Wittenbrock, and J. P. McFadden (2001), The FAST spacecraft instrument data processing unit, *Space Sci. Rev.*, *98*, 113–149, doi:10.1023/A:1013135809232.

Heelis, R. A., W. B. Hanson, and J. L. Burch 1981), AE-C observations of electric fields around auroral arcs, in *Physics of Auroral Arc Formation*, edited by S.-I. Akasofu and J. R. Kan, AGU, Washington D. C., doi:10.1029/GM025p0154.

Heppner, J. P. (1972), The Harang discontinuity in auroral belt ionospheric currents, *Geophys. Norv.*, *29*, 105–120.

Iijima, T., and T. Potemra (1976), Field-aligned currents in the dayside cusp observed by Triad, *J. Geophys. Res.*, *81*(34), 5971–5979, doi:10.1029/JA081i034p05971.

Jiang, F., R. J. Strangeway, M. G. Kivelson, J. M. Weygand, R. J. Walker, K. K. Khurana, Y. Nishimura, V. Angelopoulos, and E. Donovan (2012), In situ observations of the "pre-existing auroral arc" by THEMIS all sky imagers and the FAST spacecraft, *J. Geophys. Res.*, *117*, A05211, doi:10.1029/2011JA017128.

Karlsson, T., and G. T. Marklund (1996), A statistical study of intense low-altitude electric fields observed by Freja, *Geophys. Res. Lett.*, *23*(9), 1005–1008, doi:10.1029/96GL00773.

Koskinen, H. E. J., and T. I. Pulkkinen (1995), Midnight velocity shear zone and the concept of Harang discontinuity, *J. Geophys. Res.*, *100*(A6), 9539–9547, doi:10.1029/95JA00228.

Lessard, M. R., W. Lotko, J. LaBelle, W. Peria, C. W. Carlson, F. Creutzberg, and D. D. Wallis (2007), Ground and satellite observations of the evolution of growth phase auroral arcs, *J. Geophys. Res.*, *112*, A09304, doi:10.1029/2006JA011794.

Marklund, G. (1984), Auroral arc classification scheme based on the observed arc-associated electric field pattern, *Planet. Space Sci.*, *32*, 193–211, doi:10.1016/0032-0633(84)90154-5.

Mende, S. B., S. L. England, and H. U. Frey (2012), Plasma pressure generated auroral current system—A case study, *Geophys. Res. Lett.*, *39*, L06106, doi:10.1029/2012GL051211.

Newell, P. T., T. Sotirelis, and S. Wing (2009), Diffuse, monoenergetic, and broadband aurora: The global precipitation budget, *J. Geophys. Res.*, *114*, A09207, doi:10.1029/2009JA014326.

Nielsen, E., and R. A. Greenwald (1979), Electron flow and visual aurora at the Harang discontinuity, *J. Geophys. Res.*, *84*, 4189–4199, doi:10.1029/JA084iA08p04189.

Nishimura, Y., L. R. Lyons, V. Angelopoulos, T. Kikuchi, S. Zou, and S. B. Mende (2011), Relations between multiple auroral streamers, pre-onset thin arc formation, and substorm auroral onset, *J. Geophys. Res.*, *116*, A09214, doi:10.1029/2011JA016768.

Ohtani, S., S. Wing, P. T. Newell, and T. Higuchi (2010), Locations of night-side precipitation boundaries relative to R2 and R1 currents, *J. Geophys. Res.*, *115*, A10233, doi:10.1029/2010JA015444.

Paschmann, G., S. Haaland, and R. Treumann (2003), *Auroral Plasma Physics*, Springer, New York.

Robinson, R. M., R. R. Vondrak, K. Miller, T. Dabbs, and D. Hardy (1987), On calculating ionospheric conductances from the flux and energy of precipitating electrons, *J. Geophys. Res.*, *92*(A3), 2565–2569, doi:10.1029/JA092iA03p02565.

Samson, J. C., L. R. Lyons, P. T. Newell, F. Creutzberg, and B. Xu (1992), Proton aurora and substorm intensifications, *Geophys. Res. Lett.*, *19*(21), 2167–2170, doi:10.1029/92GL02184.

Stiles, G. S., J. C. Foster, and J. R. Doupnik (1980), Prolonged radar observations of an auroral arc, *J. Geophys. Res.*, *85*(A3), 1223–1234, doi:10.1029/JA085iA03p01223.

Timofeev, E. E., and Y. I. Galperin (1991), Convection and currents in stable auroral arcs and inverted-V's, *J. Geomagn. Geoelectr.*, *43*(Suppl), 259–274.

Vasyliunas, V. M. (1970), Mathematical models of magnetospheric convection and its coupling to the ionosphere, in *Particle and Fields in the Magnetosphere*, Springer, New York, doi:10.1007/978-94-010-3284-1_6.

Vondark, R. R. (1981), Chatanika radar measurements of the electrical properties of auroral arcs (1981), in *Physics of Auroral Arc Formation*, edited by S.-I. Akasofu and J. R. Kan, AGU, Washington, D. C.

Wang, H., H. Luhr, S. Y. Ma, and H. U. Frey (2007), Interhemispheric comparison of average substorm onset locations: Evidence for deviation from conjugacy, *Ann. Geophys.*, *25*, 989–999, doi:10.5194/angeo-25-989-2007.

Zou, S., L. R. Lyons, C.-P. Wang, A. Boudouridis, J. M. Ruohoniemi, P. C. Anderson, P. L. Dyson, and J. C. Devlin (2009), On the coupling between the Harang reversal evolution and substorm dynamics: A synthesis of Super DARN, DMSP, and IMAGE observations, *J. Geophys. Res.*, *114*, A01205, doi:10.1029/2008JA013449.

Zou, Y., Y. Nishimura, L. R. Lyons, and E. F. Donovan (2012), A statistical study of the relative locations of electron and proton auroral boundaries inferred from meridian scanning photometer observations, *J. Geophys. Res.*, *117*, A06206, doi:10.1029/2011JA017357.